Positron surface state as a spectroscopic probe for characterizing surfaces of topological insulator materials

Vincent Callewaert,[1,*] K. Shastry,[2] Rolando Saniz,[1] Ilja Makkonen,[3] Bernardo Barbiellini,[4] Badih A. Assaf,[4,5] Donald Heiman,[4] Jagadeesh S. Moodera,[6,7] Bart Partoens,[1] Arun Bansil,[4] and A. H. Weiss[2]

[1]*Department of Physics, Universiteit Antwerpen, Antwerpen 2020, Belgium*

[2]*Department of Physics, University of Texas at Arlington, Arlington, Texas 76019, USA*

[3]*Department of Applied Physics, Aalto University School of Science, P.O. Box 15100, FI-00076 Aalto, Espoo, Finland*

[4]*Department of Physics, Northeastern University, Boston, Massachusetts 02115, USA*

[5]*Département de Physique, Ecole Normale Supérieure, CNRS, PSL Research University, 24 rue Lhomond, 75005 Paris, France*

[6]*Department of Physics, MIT, Cambridge, Massachusetts 02139, USA*

[7]*Francis Bitter Magnet Laboratory, MIT, Cambridge, Massachusetts 02139, USA*

(Received 24 December 2015; revised manuscript received 16 August 2016; published 6 September 2016)

Topological insulators are attracting considerable interest due to their potential for technological applications and as platforms for exploring wide-ranging fundamental science questions. In order to exploit, fine-tune, control, and manipulate the topological surface states, spectroscopic tools which can effectively probe their properties are of key importance. Here, we demonstrate that positrons provide a sensitive probe for topological states and that the associated annihilation spectrum provides a technique for characterizing these states. Firm experimental evidence for the existence of a positron surface state near Bi_2Te_2Se with a binding energy of $E_b = 2.7 \pm 0.2$ eV is presented and is confirmed by first-principles calculations. Additionally, the simulations predict a significant signal originating from annihilation with the topological surface states and show the feasibility to detect their spin texture through the use of spin-polarized positron beams.

DOI: 10.1103/PhysRevB.94.115411

I. INTRODUCTION

Quickly after their initial discovery, topological insulators (TIs) were recognized to hold significant potential for new technological applications and as a playground for fundamental physics [1]. An intrinsic challenge with TIs, which arises due to the fact that their interesting properties originate from Dirac states located in a nanoscopic layer near the surface, remains to separate the fingerprint of the topological surface states from the bulk behavior of the sample. Highly surface-sensitive techniques, such as angle-resolved photoemission spectroscopy and scanning tunneling microscopy have thus proven to be indispensable tools to establish the existence of the gapless states in several systems and to confirm various predicted quasiparticle properties [2].

In this article, we demonstrate that positrons provide a highly surface-sensitive probe for the topological Dirac states. Since positron annihilation spectroscopy (PAS) techniques with measurements of the two-dimensional angular correlation of the annihilation radiation (2D-ACAR) in particular are well suited to measure both the low- and the high-momentum components of the annihilating electronic states without complication of matrix element effects, they can provide useful information on the Dirac state orbitals. Our calculations show that spin-polarized positron beams can additionally resolve the spin textures associated with the topological states, owing to the predominant annihilation between particles with opposite spins [3].

In Sec. II, we present the experimental evidence for the existence of a bound positron state at the surface of the TI Bi_2Te_2Se and the measured binding energy [4]. Section III contains a discussion of the theory and computational details used in our first-principles investigation. In Sec. IV, we show that the theory confirms the experimental interpretation and predicts a significant overlap between the positron and the topological states. We also demonstrate that spin-polarized positron measurements can reveal the spin structure at the surface. In Sec. V we summarize the results and discuss possible applications and advantages of PAS over other spectroscopic techniques.

II. EXPERIMENTAL RESULTS

Our Bi_2Te_2Se films are grown by molecular-beam epitaxy on Si (111). The substrates are etched in hydrofluoric acid prior to loading in vacuum. A stoichiometric 2:2:1 Bi:Te:Se flux ratio is used. The substrate temperature is fixed at 200 °C during the growth. The films used in this study are typically 40-nm thick. A 100-nm Se cap is then deposited *in situ* on the sample surface after cooling down the substrate to room temperature. The capping layer protects the film surface from oxidation and atmospheric contaminants.

X-ray diffraction is systematically used to characterize the samples as briefly discussed in Ref. [5]. The *c*-axis lattice constant for the film used in this paper is found to be equal to 30.10 ± 0.03 Å. Energy dispersive x-ray spectroscopy confirmed stoichiometry within a 5% error on samples resulting from an identical growth.

The samples are then transferred to the experimental positron chamber. In order to decap the samples, the protective Se layer is evaporated under UHV conditions, prior to the positron annihilation experiment. A heater button is placed behind the sample in a holder, and a suitable current was passed to heat the sample for 20 min at 200 °C. This

*vincent.callewaert@uantwerpen.be

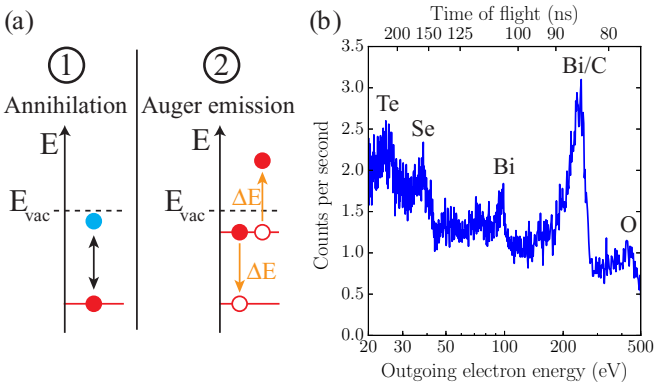

FIG. 1. (a) Schematic of the PAES mechanism. In the first step, a positron (blue) annihilates with an electron (red) occupying a core level and creates a highly unstable hole. In the second step, an electron from a higher level fills this hole and transfers the energy difference between the two levels to a second electron. If the energy difference is sufficiently large and the second electron is close enough to the surface, it can traverse the surface dipole and escape from the sample. The measured outgoing electron energy corresponds with the transferred energy in the Auger process minus the energy difference between the second electron's state and the vacuum level. (b) Results of the PAES measurements on the Bi_2Te_2Se sample in which Auger signals from the different elements are indicated.

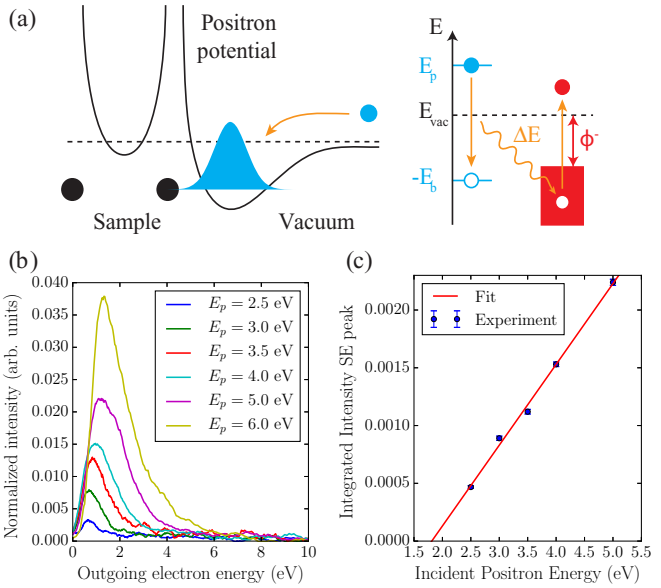

FIG. 2. (a) Schematic of the AMPS mechanism. The left part of the diagram shows the incident positron (blue) that drops in the image potential well. In this process, the positron transfers an energy ΔE, determined by the incident kinetic-energy E_p and the binding energy of the SS E_b, to an electron of the system through a virtual photon as indicated in the right part of the figure. If the energy difference is larger than the electronic work-function ϕ^-, the electron can escape to the vacuum. (b) The measured low-energy Auger signals for the Bi_2Te_2Se sample. The outgoing electron energy is determined by the transferred energy ΔE minus the required energy to escape from the sample. The different lines show the result for varying energies of the incident positrons. (c) The integrated peak amplitudes of the low-energy Auger signal associated with the AMPS mechanism as a function of the incident positron energy.

procedure is similar to the decapping sequence used in Ref. [6]. The technical details concerning the setup of the positron experiments can be found in Ref. [4] and references therein.

Positrons annihilate predominantly with the valence electrons, but the small fraction that annihilates with core electrons produces highly unstable core holes, which are filled by the Auger process. Therefore, if positrons annihilate in a surface state (SS), positron-induced Auger-electron spectroscopy (PAES) provides a particularly clean method to determine the composition of the surface, free from a secondary electron background [7]. A schematic of the process is drawn in Fig. 1(a). Results of PAES experiments from the TI Bi_2Te_2Se surface are shown in Fig. 1(b) where signals from Bi, Te, Se, C, and O can be identified; the latter two are caused by the presence of a small concentration of contaminants adsorbed on the surface [4]. These results reveal the presence of a bound positron SS. Were this not the case, positrons would either get trapped between the blocks of quintuple layers (QLs) of the material or would be reemitted before they annihilate. Since the extent of one QL block is about 10 Å, which corresponds roughly to the mean-free path of a 60-eV electron, any Auger signal coming from below the first QL is too weak to be detected. Thus, the fact that the annihilation-induced Auger peak intensities are observable is clear evidence that the positron is in a state localized at the surface at the time it annihilates.

Auger mediated positron sticking (AMPS) experiments provide an independent proof for the existence of the SS and allow us to determine its binding energy [8]. In the AMPS mechanism, the excess energy from a positron dropping into the image potential well is transferred to a valence electron. This can result in the emission of an Auger electron if the energy difference between the positron SS and the initial state, determined by the incident positron's kinetic energy, is larger than the electron work function [8]. The maximum kinetic energy of the Auger electrons is then given by $E_{\max} = E_p + E_b - \phi^-$, where E_p is the energy of the incident positron, E_b is the binding energy of the positron surface state, and ϕ^- is the electron work function. Figure 2(a) illustrates the AMPS mechanism schematically. The observed increase in amplitude of the Auger signal at low energies as the energy of the incident positrons is increased is shown in Fig. 2(b), and it confirms the presence of the SS. Knowing the electron work function, the binding energy of the SS can be determined from the positron energy threshold value for Auger-electron emission: $E_{Th} = E_p$ for which $E_{\max} = 0$. The linear fit shown in Fig. 2(c) yields $E_{Th} = 1.8$ eV. Next, by considering the measured activation energy $E_a = 0.4$ eV for positronium (Ps) desorption from the surface [4], one can eliminate the electron work function using the expression [9] $E_a = E_b + \phi^- - 6.80$ eV, which gives a binding energy of $E_b = 2.7 \pm 0.2$ eV (Ref. [4]).

III. THEORY AND COMPUTATIONAL DETAILS

Our first-principles calculations are carried out in the zero-positron-density limit of the two-component electron-positron density functional theory (2CDFT) [10,11]. In this limit, which

is exact in the case of a delocalized positron in a perfect crystal or at a surface, the electron density remains unperturbed by the presence of the positron. The computations thus consist of an electronic and positronic ground-state calculation which are performed subsequently.

A. Electronic structure

The electronic ground state is obtained using the projector-augmented-wave (PAW) method [12] as implemented in the VASP software package [13–15]. Electron exchange-correlation effects are treated using the Perdew-Burke-Ernzerhof (PBE) functional [16], and spin-orbit coupling is included in the computations. The kinetic-energy cutoff for the plane-wave expansion of the wave functions is set at 275 eV. For the bulk calculations, we use the rhombohedral unit cell with a Γ-centered $11\times11\times11$ **k** grid in combination with a Gaussian smearing of width 0.1 eV. In the surface calculations, we use a slab geometry with a vacuum of 15 Å to avoid spurious interactions between periodic images. Here, the calculations are performed with a Γ-centered **k** grid with $11\times11\times1$ points in the hexagonal unit cell in combination with a Gaussian smearing of 0.1 eV. We used the experimental lattice parameters in all our calculations [17].

B. Positron state

The effective potential for the positron in the zero-density limit of the 2CDFT is determined by the Coulomb interaction with the nuclei, the Hartree interaction with the electron density, and the electron-positron correlation potential. The latter is usually described with the local density approximation (LDA) or the generalized gradient approximation (GGA), which give reliable results for bulk systems. A fundamental limitation of these semilocal approximations is that they always describe the formation of Ps^- in the limit of a dilute electron gas. In the case of a surface, however, the correct limit is given by the image potential [18] $-1/4(z-z_0)$, where z denotes the distance to the surface and z_0 represents the image potential reference plane. We impose this limit in the vacuum region by considering the corrugated mirror model [19] in which the image potential is constructed to follow the same isosurfaces as the electron density. In the vacuum region $z > z_0$, we take the least negative of the LDA potential [20] and the image potential. The strength of the image potential is given by [19]

$$V_{\mathrm{im}}(\mathbf{r}) = -\frac{1}{4\{z_{\mathrm{eff}}[n^-(\mathbf{r})] - z_0\}}, \tag{1}$$

where $n^-(\mathbf{r})$ is the electron density and the effective distance to the surface is determined by

$$z_{\mathrm{eff}}[n^-(\mathbf{r})] = \int_{z_0}^{\infty} dz' z' \delta[n^-(\mathbf{r}) - \langle n^-\rangle(z')]. \tag{2}$$

Here, $\langle n^-\rangle$ is the electron density averaged over the planes parallel to the surface, and δ denotes the Dirac δ function. We approximate the image potential reference plane z_0 by the background edge position, which is determined by the position outside the surface where the electron density starts decaying exponentially.

We used the MIKA/Doppler package [21] to obtain the positron ground state. These calculations are performed in an all-electron way in the sense that a superposition of free atomic core quantities, e.g., density and the Hartree potential, are added to the self-consistent valence electron properties. The Kohn-Sham equations for the positron are solved on a real-space grid using a Rayleigh multigrid implementation [22,23].

C. Electron-positron momentum density

The goal of the present paper is to investigate whether PAS can be used to measure the properties of the TI's Dirac states. We thus need to calculate the electron-positron momentum density, which contains information about a sample's electronic structure and determine if it contains a clear fingerprint of the topological states.

Due to strong spin-orbit coupling in Bi_2Te_2Se the electronic wave functions are not collinear. Hence, we present a generalization of the theory of electron-positron momentum-density calculations to deal with noncollinear wave functions.

Spin-polarized positron annihilation measurements exploit the fact that the two-γ annihilation only occurs for electron-positron pairs in a singlet state. If one specifies the initial spin of the positron, this translates to saying that the positron will only annihilate with electrons of the opposite spin. The magnetization of the electron-positron momentum density along a specified axis can thus be obtained by taking the difference between spectra obtained by aligning the positrons parallel and antiparallel to that axis. As long as the electron and positron spins are good quantum numbers, i.e., they are position independent, the effect of the spin is easily taken into account by realizing that the positron will be in a singlet state with exactly half of the electron states with the opposite spin. In systems where the spin cannot be considered a good quantum number, however, a more careful examination is required. In general, we can write the momentum density of the annihilating electron-positron pairs as [24,25]

$$\rho(\mathbf{p}) = 4\pi r_e^2 c \sum_j g_j \sum_{s_e,s_p} \left| \int d\mathbf{r}\, e^{-i\mathbf{p}\cdot\mathbf{r}} \hat{S}^s \alpha_j(\mathbf{r},s_e;\mathbf{r},s_p) \right|^2, \tag{3}$$

where $|\alpha_j\rangle$ are the natural geminals which diagonalize the reduced two-body density matrix, sometimes also referred to as electron-positron pairing wave functions, and the g_j are their occupation numbers. The spins of the electron and positron in the geminal are denoted by s_e and s_p, respectively, and j represents a set of quantum numbers (excluding the spin of the particles). The factor $4\pi r_e^2 c$ with r_e as the classical electron radius and c as the speed of light, is the annihilation rate constant [26]. The operator $\hat{S}^s = 1 - \frac{1}{2}\hat{S}^2$, where $\hat{S}$ is the total spin operator for the electron-positron pair, projects on the singlet state. For the purpose of notation as well as practical calculations, it is convenient to define

$$A_{j,s_e,s_p}(\mathbf{p}) = \int d\mathbf{r}\, e^{-i\mathbf{p}\cdot\mathbf{r}} \alpha_j(\mathbf{r},s_e;\mathbf{r},s_p), \tag{4}$$

as well as the matrix,

$$\Gamma_j(\mathbf{p}) = \begin{pmatrix} |A_{j,\uparrow\downarrow}(\mathbf{p})|^2 & A_{j,\uparrow\downarrow}(\mathbf{p})A^*_{j,\downarrow\uparrow}(\mathbf{p}) \\ A_{j,\downarrow\uparrow}(\mathbf{p})A^*_{j,\uparrow\downarrow}(\mathbf{p}) & |A_{j,\downarrow\uparrow}(\mathbf{p})|^2 \end{pmatrix}. \tag{5}$$

In measurements with unpolarized positron beams, the positron has statistically a 50% chance to be either in the spin-up or spin-down state. In this case, upon evaluation of Eq. (3), the off-diagonal terms of $\Gamma_j(\mathbf{p})$ drop since the geminals with opposite spin orientations, e.g., $\alpha_j(\mathbf{r},\uparrow;\mathbf{r},\downarrow)$ and $\alpha_j(\mathbf{r},\downarrow;\mathbf{r},\uparrow)$, are not simultaneously occupied. The result for the momentum density then becomes

$$\rho(\mathbf{p}) = \pi r_e^2 c \sum_j g_j \mathrm{Tr}[\Gamma_j(\mathbf{p})], \tag{6}$$

where $\mathrm{Tr}[\cdots]$ denotes taking the trace. In case the positron beam is perfectly polarized parallel or antiparallel to the z axis, we obtain

$$\rho_z^{\uparrow}(\mathbf{p}) = 2\pi r_e^2 c \sum_j g_j |A_{j,\uparrow\downarrow}(\mathbf{p})|^2, \tag{7}$$

and

$$\rho_z^{\downarrow}(\mathbf{p}) = 2\pi r_e^2 c \sum_j g_j |A_{j,\downarrow\uparrow}(\mathbf{p})|^2, \tag{8}$$

respectively. The magnetization along the z axis is obtained by taking the difference between these two spectra and can conveniently be written as

$$\rho_z(\mathbf{p}) = 2\pi r_e^2 c \sum_j g_j \mathrm{Tr}[\sigma_z \Gamma_j(\mathbf{p})], \tag{9}$$

where σ_z denotes the Pauli matrix. Analogous observations can be made for a positron polarized along the different axes, thus we can write in general,

$$\rho_i(\mathbf{p}) = 2\pi r_e^2 c \sum_j g_j \mathrm{Tr}[\sigma_i \Gamma_j(\mathbf{p})], \tag{10}$$

where $i = \{x,y,z\}$ and σ_i are the Pauli matrices. A detailed derivation of the above formulas can be found in the Supplemental Material [27].

In electron-positron momentum-density calculations based on the 2CDFT, one assumes that the natural geminals can be written in terms of a product of the electron and positron single-particle Kohn-Sham orbitals ψ^-_{j,s_e} and $\psi^+_{s_p}$ where the positron is assumed to reside in its ground state and the occupation numbers of the electronic orbitals replace those of the natural geminals g_j. Electron-positron correlation effects are included by introducing a multiplicative term γ, i.e., the enhancement factor, which can be state and/or space dependent. We thus have

$$\alpha_j(\mathbf{r},s_e;\mathbf{r},s_p) = \sqrt{\gamma_{j,s_e,s_p}(\mathbf{r})}\psi^-_{j,s_e}(\mathbf{r})\psi^+_{s_p}(\mathbf{r}). \tag{11}$$

Note that, in general, it is justified to consider the positron wave function to be collinear even though the electronic states are not. Indeed, electron-positron spin-spin interactions are small and generally neglected in PAS studies, and positrons stay too far away from the nuclei to experience any significant spin-orbit interaction. We thus assume that the orbital part of the positron wave function is independent of the chosen spin polarization: $\psi^+_{s_p}(\mathbf{r}) = \psi^+(\mathbf{r})\chi_{s_p}$, where χ_{s_p} denotes a two-component spinor for the positron. Note that for the calculation of the momentum density from Eqs. (6) and (10), we have to set $\psi^+_{\uparrow}(\mathbf{r}) = \psi^+_{\downarrow}(\mathbf{r})$ instead of explicitly setting a polarization.

In our calculations, we consider the state-dependent enhancement factors [28]: $\gamma_{j,s_e,s_p} = \lambda^{\mathrm{LDA}}_{j,s_e,s_p}/\lambda^{\mathrm{IPM}}_{j,s_e,s_p}$. The λ's denote the partial annihilation rates in the LDA and independent particle model (IPM), respectively, and the former is calculated as

$$\lambda^{\mathrm{LDA}}_{j,s_e,s_p} = \pi r_e^2 c \int d\mathbf{r} \left|\psi^-_{j,s_e}(\mathbf{r})\right|^2 \left|\psi^+_{s_p}(\mathbf{r})\right|^2 \gamma[n^-(\mathbf{r})], \tag{12}$$

with $\gamma[n^-(\mathbf{r})]$ as the LDA enhancement factor parametrized by Drummond *et al.* [29]. The IPM annihilation rates are obtained by setting $\gamma[n^-(\mathbf{r})] = 1$.

The high-momentum components of the wave functions are important to accurately calculate the electron-positron momentum density. It is thus necessary to use the all-electron wave functions in the above formulas instead of the soft pseudowave functions, i.e., we explicitly perform the PAW transformation [12],

$$|\psi^-\rangle = |\tilde{\psi}^-\rangle + \sum_i (|\phi^-_i\rangle - |\tilde{\phi}^-_i\rangle)\langle \tilde{p}_i|\tilde{\psi}^-\rangle. \tag{13}$$

Here, $|\tilde{\psi}^-_j\rangle$ are the soft pseudowave functions, $\langle \tilde{p}_i|$ are the projectors, and $|\phi^-_i\rangle$ and $|\tilde{\phi}^-_i\rangle$ are the localized all-electron partial waves and soft pseudo partial waves of the ions, respectively. The details on how we performed this transformation can be found in Refs. [21,24].

D. Positronium model

We can theoretically determine the activation energy for Ps desorption from Bi_2Te_2Se of which the experimental results are described in Ref. [4] by calculating the particle's binding energy to the surface. In order to model the Ps state, we consider the Schrödinger equation for a neutral particle in an effective potential well [30]. Here, the effective potential outside the surface is determined by an attractive and a repulsive contribution. The repulsive contribution due to the overlap of the electron of Ps with electrons of the material is given by

$$V_R(z) = |\phi^{\mathrm{Ps}}| e^{-(z-z_0)/\lambda}, \tag{14}$$

where ϕ^{Ps} is the Ps work function, z_0 is the background edge position, and λ is the characteristic length of the electron-density decay outside the surface. The Ps work function can be calculated by taking the sum of the work functions of the constituent particles minus their binding energy: $\phi^{\mathrm{Ps}} = \phi^+ + \phi^- - 0.25$ Ha. The attractive part of the interaction is given by the van der Waals interaction and can be written as

$$V_{vdW}(z) = -\frac{C}{(z-z_0')^3} F[(z-z_0')/\lambda], \tag{15}$$

where the strength of the interaction is given by the expression [31],

$$C = \frac{\hbar}{4\pi}\int_0^{\infty} d\omega\, \alpha(i\omega)\left(\frac{\epsilon(i\omega)-1}{\epsilon(i\omega)+1}\right). \tag{16}$$

The bulk dielectric function ϵ at imaginary frequencies can be obtained by first evaluating the dielectric function at real frequencies, which is readily calculated from first principles in the random-phase approximation, and then applying analytic continuation. The Ps polarizability α can be obtained from the analytic expression for H-like atoms, given in Ref. [32],

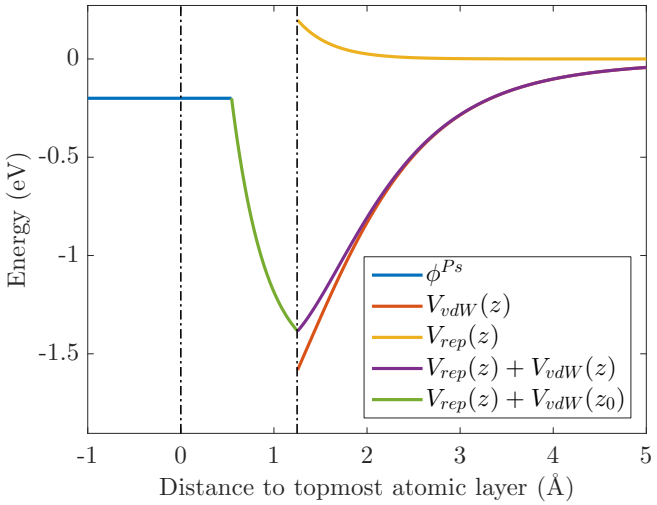

FIG. 3. Potential obtained for the Ps model with the values for C, z_0, λ, and ϕ^+ mentioned in the discussion. For the electronic work function, we took $\phi^- = 4.612$ eV, which gives a Ps work function of $\phi^{\rm Ps} = 0.2$ eV and lies in the middle of the range of values for which the model gives an activation energy in good agreement with the experimental result.

by rescaling. Indeed, the Ps problem can be solved by going to the center-of-mass coordinates, which then yield the same equations as for the H atom. The only differences are that the Bohr radius is twice as large and the ionization energy is half the value of that of H. The analytic damping function F for which we take expression (17) of Ref. [33] describes the saturation of the van der Waals interaction as the particle draws closer to the surface and regularizes the divergence at the reference plane position $z = z_0'$. The reference plane position can in principle take another value than the background edge position but since they are both, in the case of an elementary metal with lattice parameter a, located close to $a/2$, we make the approximation $z_0' = z_0$. For $z < z_0$, we extend the repulsive interaction and add $V_{vdW}(z_0)$ to ensure the continuity of the potential with a cutoff set by the Ps work function,

$$V(z) = \min\{\phi^{\rm Ps}, V_R(z) + V_{vdW}(z_0)\}\Theta(z < z_0) + \{V_R(z) + V_{vdW}(z)\}\Theta(z \geqslant z_0), \quad (17)$$

where $\Theta(\dots)$ is the Heaviside function. The different contributions to the potential are shown in Fig. 3. The Ps state and its energy are obtained by solving the resulting Schrödinger equation,

$$-\frac{\psi''}{4} + V(z)\psi = E\psi. \quad (18)$$

IV. COMPUTATIONAL RESULTS

We start our discussion of the computations by showing that the measured Ps activation energy $E_a = 0.4$ eV [4] is consistent with the theoretical predictions. We take the activation energy to be equal to the ground-state energy predicted by the Ps model discussed in the previous section. For the parameters in the model, we find that the van der Waals interaction strength evaluates to $C = 2.306$ eV Å^3 and from the electronic and positronic work functions $\phi^- = 4.904$ and $\phi^+ = 2.392$ eV, we obtain $\phi^{\rm Ps} = 0.493$ eV. The values for the background edge position and the characteristic length of the electron-density decay in the vacuum region are given by $z_0 = 1.250$ and $\lambda = 0.365$ Å. Using these values, the model predicts that the Ps forms a delocalized state in the bulk of the material. We note, though, that the experimental value for the electronic work function $\phi^- = 4.5$ eV is lower than the theoretical one. It is thus sensible to consider the outcome of the model for $\phi^- \in [4.5,4.9]$ eV. Over the range of $\phi^- = 4.90$ to $\phi^- = 4.72$ eV, we find that the ground state gradually shifts from the bulk to the surface. To determine when we have a surface state, we set the criterion that the Ps density should decay below 1% of its maximum value beyond the first QL block inside the material. In the range of $\phi^- \in [4.52,4.72]$ eV, the Ps model predicts a surface state with a binding energy of $E_{\rm Ps} = 0.40 \pm 0.05$ eV, in good agreement with the experimental results.

Next, we investigate the predictions of the 2CDFT calculations to determine whether they support the proposed interpretation of the PAES and AMPS experiments. Our first observation is that the positron in its ground state indeed resides in the surface's image potential well rather than the gaps in between the QLs, which also act as strong positron traps. We obtain the binding energy of the positron by taking the difference between the vacuum level and the positron's chemical potential. The vacuum level is determined in the usual way by the taking the value of the Hartree potential in the middle of the vacuum region. We find that the positron SS has a binding energy of $E_b = 2.69$ eV, in excellent agreement with the measured value. We find that the lifetime evaluates to $\tau = 309.25$ ps. This value seems reasonable compared with the lifetime of 340–380 ps measured for positrons trapped at the surface of colloidal PbSe quantum dots [34]. On the other hand, a lifetime of 580 ps has been determined for positrons trapped at an Al surface [35], which cannot be reproduced within the LDA approximation [19]. One workaround suggested in literature is to set the enhancement factor to zero for $z > z_0$, i.e., assume that the positron will not annihilate in the vacuum region [36]. We find, though, that this operation makes the result for the lifetime depend sensitively on the value for the image potential reference plane z_0. For this reason, as well as the scarcity of experimental data that show this operation is justified, the rest of our calculations have been carried out without modifying the LDA enhancement factor.

Now that the calculations confirmed the existence of the bound positron SS, we turn to the important question of the extent to which this SS overlaps with the Dirac cone electrons. This overlap is of central importance because it determines the annihilation rate of the positron with the electrons occupying the topological states and thus the sensitivity with which positron annihilation spectroscopy can probe the Dirac states. This can be seen from Eq. (12) where the partial annihilation rate is determined by the sum over all λ_j where j represents a state on the cone.

The computed densities of the positron SS, ρ^+, and the topological Dirac states $\rho^-_{\rm Dirac}$ are shown in Fig. 4. The density of the topological states is obtained by summing the one-particle densities for all states on the cone between

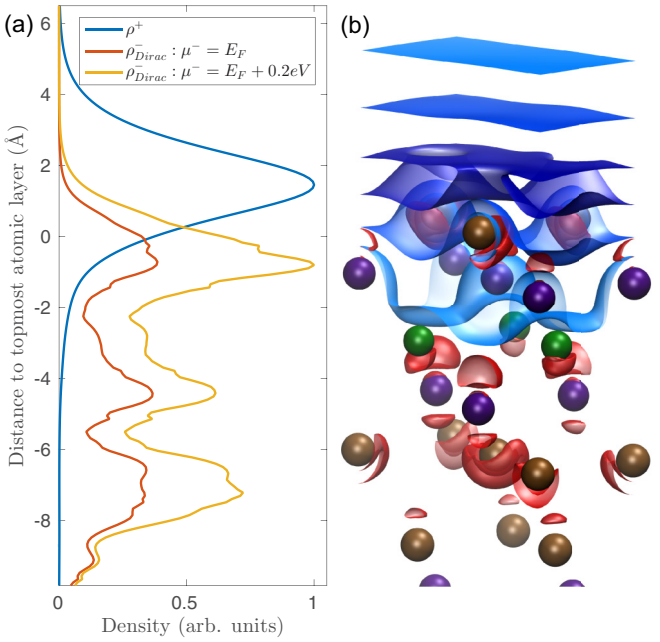

FIG. 4. Overlap of the positron SS with the Dirac states. (a) Planar average of the positron (blue) and electron (red/yellow) densities associated with the Dirac states below the Fermi energy for two different values of the chemical potential μ^-. (b) Density of the topological surface state and the positron in the same spatial region as panel (a). The progressively lighter blue isosurfaces show the positron density at 80%, 20%, and 2% of the maximum value, respectively, and the red isosurfaces show the electronic charge density associated with the electron states on the Dirac cone below the Fermi level at 10% of the maximum value. The Bi, Te, and Se atoms are shown in purple, brown, and green colors, respectively.

the Dirac point and a specific value for the electron chemical potential μ^-. Although the positron is seen to probe only the topmost atomic layers of the material, it still penetrates the material sufficiently to have a significant overlap with the Dirac states. Moreover, the left panel of Fig. 4 shows that the overlap with the Dirac states changes sensitively depending on the population of the Dirac states near the Fermi level. Our calculations of the momentum density, discussed below, further demonstrate that this underlying overlap translates into a clear signal coming from the annihilation of the positron with the Dirac fermions.

A partially filled energy band when it crosses the Fermi energy gives rise to a break in the electron-momentum density, which is the basis of the measurement of Fermi surfaces in materials via 2D-ACAR experiments. A standard procedure for enhancing the Fermi-surface signal in the spectrum is the Lock-Crisp-West (LCW) map obtained by folding all the higher-momentum (Umklapp) contributions into the first Brillouin zone [37]. Figure 5 shows the calculated LCW map together with a cut along Γ-M over a range of values of the electron chemical potential, which simulates different doping levels of the Dirac cone. The evolution of the plateau around the Γ point clearly indicates the sensitivity of the positron to the Dirac cone states. The relative drop in intensity between 5% and 7% at the Fermi momentum compares favorably with, for example, the 1% drop found for the $Nd_{2-x}Ce_xCuO_{4-\delta}$ high-T_c superconductor in which 2D-ACAR experiments have been shown previously to be viable in detecting Fermi-surface sheets due to Cu-O planes [38].

A topic which has drawn considerable interest in the case of topological insulators is the spin-momentum locking of the topological states. Measurements using spin-polarized positron beams exploit the fact that a two-photon decay is only possible between electrons and positrons with opposite spins [3]. In recent work, spin effects in the electronic structure of simple ferromagnets were observed using differences between the Doppler broadening of the annihilation radiation measured with positrons aligned parallel and antiparallel to a polarizing magnetic field [39]. In a similar ACAR experiment, Weber *et al.* [40] successfully resolved the spin-dependent Fermi surface of the ferromagnetic Heusler compound Cu_2MnAl. This motivates us to investigate whether spin-polarized positrons can be used to detect the spin structure of the topological states at the surface. The signal from the Fermi surface can be extracted from the LCW map by taking the difference between the signal obtained at different

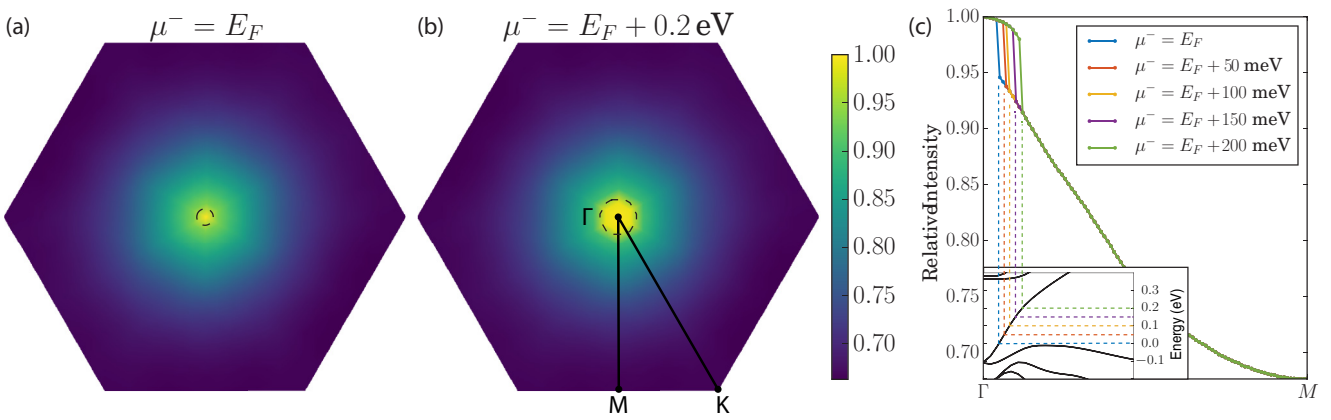

FIG. 5. Theoretical momentum densities. (a) LCW map with the chemical potential located at the Fermi level. (b) LCW map with the chemical potential raised by 0.2 eV. The dashed lines denote the location of the Fermi surface as derived from the electronic band structure. (c) High-resolution cuts through the LCW map along the Γ-M direction for different values of the chemical potential. The inset shows the band structure near the Fermi level ($E_F = 0.0$ eV).

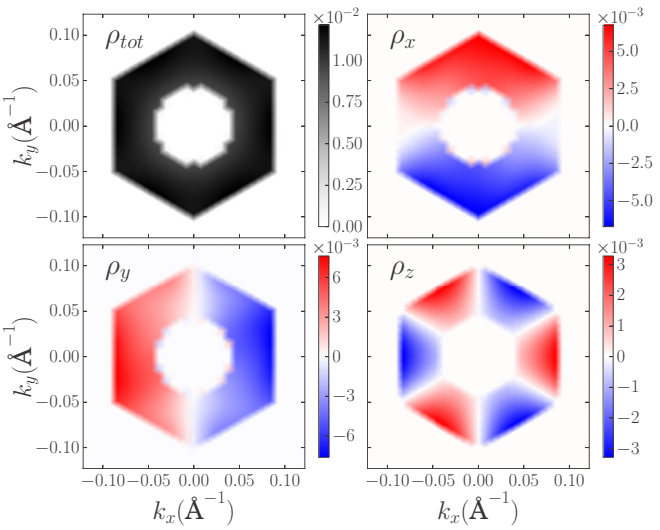

FIG. 6. Difference between the LCW maps obtained with different doping levels of the Dirac cone: $\mu^- = E_F + 0.2$ eV and $\mu^- = E_F$. The top left pane of the figure shows the total amplitude of the LCW map. The top right, bottom left, and bottom right figures show the magnetization components along the x, y, and z axes, respectively. We only show the result zoomed in around the Γ point as the difference between the LCW maps is exactly zero in the rest of the Brillouin zone. The inner and othermost edges of the nonzero part in the plots correspond with the dashed lines shown in Figs. 5(a) and 5(b), respectively. The length of the reciprocal axes is $|\mathbf{b}| = 1.688$ Å^{-1}, and the amplitudes are given in ps^{-1} Å^2. (It is readily seen that the units of the LCW map are in ps^{-1} Å^2 by realizing that the integral over the LCW map yields the positron's annihilation rate, or in the case of the magnetic LCW maps, the difference in annihilation rate between two measurements with opposite spin polarizations for the positron.)

doping levels. In Fig. 6, we show the results obtained by taking the difference between the LCW maps obtained with $\mu^- = E_F + 0.2$ eV and $\mu^- = E_F$ in the vicinity of the Γ point. As expected, we see the plateau due to the extra occupation of the cone in the total amplitude. Our results for the magnetization along the x and y directions agree well with the results obtained in several studies of various tetradymite TIs [41–44], which all predict a clockwise rotation of the spin. We see that the z component of the magnetization increases gradually away from the Γ point. This out-of-plane component develops due to the hexagonal warping of the Dirac cone as pointed out by Fu [45]. We note that the difference in amplitude for the magnetic components is quite pronounced with regard to the Fermi-surface signal. Indeed, we find that the signal from the magnetization is about half that of the Fermi-surface signal obtainable with an unpolarized beam. This means that the magnetization signal still constitutes a promising 2%–4% of the total signal. We note, though, that in real experiments, positron beams are not perfectly polarized as we have assumed in our calculations. Thus, in experiment, a proper weighting has to be performed which will lead to a smaller signal.

V. CONCLUSION AND OUTLOOK

Our study establishes the existence of a positron surface state near the topological insulator Bi_2Te_2Se. The results of our calculations show that this surface state can be exploited as a spectroscopic characterization tool for probing surfaces of topological materials. Since a significant fraction of positrons annihilate with electrons occupying Dirac cone states, 2D-ACAR experiments should be able to measure their momentum distribution with high precision [46] and thus obtain information concerning the nature of the Dirac states which is complementary to that accessed through angle-resolved photoemission, scanning tunneling, and other surface-sensitive spectroscopies without the complications of related matrix element effects [47]. PAES and Doppler broadening of the annihilation radiation [48] measurements can, in turn, be used to characterize the chemical composition of surfaces. In combination with 2D-ACAR experiments, these positron spectroscopies could be exploited to determine effects of various surface impurities on the topological states in addition to the role of bulk defects [49]. Now that our study identified a positron surface state, positron spectroscopies can prove valuable for the characterization of nanostructured topological insulators. Indeed, positrons have been shown to act as effective self-seeking probes for nanocrystal surfaces without requiring the preparation of single-crystal specimens [50], whereas the applicability of conventional spectroscopic techniques is limited. Finally, our calculations show that the spin textures of the Dirac states should be accessible through 2D-ACAR measurements using a spin-polarized positron beam since positrons predominantly annihilate with electrons of the opposite spin [3,39,40].

ACKNOWLEDGMENTS

I.M. acknowledges discussions with M. Ervasti and A. Harju. V.C. and R.S. were supported by the FWO-Vlaanderen through Project No. G. 0224.14N. The computational resources and services used in this paper were, in part, provided by the VSC (Flemish Supercomputer Center) and the HPC infrastructure of the University of Antwerp (CalcUA), both funded by the Hercules Foundation and the Flemish Government (EWI Department). I.M. acknowledges financial support from the Academy of Finland (Projects No. 285809 and No. 293932). The work at Northeastern University was supported by the U.S. Department of Energy (DOE), Office of Science, Basic Energy Sciences Grant No. DE-FG02-07ER46352 and benefited from Northeastern University's Advanced Scientific Computation Center (ASCC) and the NERSC supercomputing center through DOE Grant No. DE-AC02-05CH11231. K.S. and A.W. acknowledge financial support from the National Science Foundation through Grants No. DMR-MRI-1338130 and No. DMR-1508719. D.H. received financial support from the National Science Foundation (Grant No. ECCS-1402738). J.S.M. was supported by the STC Center for Integrated Quantum Materials under NSF Grants No. DMR-1231319, No. DMR-1207469, and ONR Grant No. N00014-13-1-0301. B.A.A. also acknowledges support from the LabEx ENS-ICFP Grant No. ANR-10-LABX-0010/ANR-10-IDEX-0001-02 PSL.

[1] M. Z. Hasan and C. L. Kane, Rev. Mod. Phys. **82**, 3045 (2010); A. Bansil, H. Lin, and T. Das, *ibid.* **88**, 021004 (2016); J. E. Moore, Nature (London) **464**, 194 (2010); A. R. Mellnik, J. S. Lee, A. Richardella, J. L. Grab, P. J. Mintun, M. H. Fischer, A. Vaezi, A. Manchon, E.-A. Kim, N. Samarth, and D. C. Ralph, *ibid.* **511**, 449 (2014); V. Mourik, K. Zuo, S. M. Frolov, S. R. Plissard, E. P. A. M. Bakkers, and L. P. Kouwenhoven, Science **336**, 1003 (2012).

[2] D. Hsieh, D. Qian, L. Wray, Y. Xia, Y. S. Hor, R. J. Cava, and M. Z. Hasan, Nature (London) **452**, 970 (2008); D. Hsieh, Y. Xia, D. Qian, L. Wray, J. H. Dil, F. Meier, J. Osterwalder, L. Patthey, J. G. Checkelsky, N. P. Ong, A. V. Fedorov, H. Lin, A. Bansil, D. Grauer, Y. S. Hor, R. J. Cava, and M. Z. Hasan, *ibid.* **460**, 1101 (2009); P. Roushan, J. Seo, C. V. Parker, Y. S. Hor, D. Hsieh, D. Qian, A. Richardella, M. Z. Hasan, R. J. Cava, and A. Yazdani, *ibid.* **460**, 1106 (2009); Y. Xia, D. Qian, D. Hsieh, L. Wray, A. Pal, H. Lin, A. Bansil, D. Grauer, Y. S. Hor, R. J. Cava, and M. Z. Hasan, Nat. Phys. **5**, 398 (2009).

[3] S. Berko and J. Zuckerman, Phys. Rev. Lett. **13**, 339 (1964).

[4] K. Shastry, A. H. Weiss, B. Barbiellini, B. A. Assaf, Z. H. Lim, P. V. Joglekar, and D. Heiman, J. Phys.: Conf. Ser. **618**, 012006 (2015).

[5] B. A. Assaf, T. Cardinal, P. Wei, F. Katmis, J. S. Moodera, and D. Heiman, Appl. Phys. Lett. **102**, 012102 (2013).

[6] D. Zhang, A. Richardella, D. W. Rench, S.-Y. Xu, A. Kandala, T. C. Flanagan, H. Beidenkopf, A. L. Yeats, B. B. Buckley, P. V. Klimov, D. D. Awschalom, A. Yazdani, P. Schiffer, M. Z. Hasan, and N. Samarth, Phys. Rev. B **86**, 205127 (2012).

[7] A. Weiss, R. Mayer, M. Jibaly, C. Lei, D. Mehl, and K. G. Lynn, Phys. Rev. Lett. **61**, 2245 (1988).

[8] S. Mukherjee, M. P. Nadesalingam, P. Guagliardo, A. D. Sergeant, B. Barbiellini, J. F. Williams, N. G. Fazleev, and A. H. Weiss, Phys. Rev. Lett. **104**, 247403 (2010).

[9] S. Chu, A. P. Mills, and C. A. Murray, Phys. Rev. B **23**, 2060 (1981).

[10] B. Chakraborty and R. W. Siegel, Phys. Rev. B **27**, 4535 (1983).

[11] E. Boronski and R. M. Nieminen, Phys. Rev. B **34**, 3820 (1986).

[12] P. E. Blöchl, Phys. Rev. B **50**, 17953 (1994).

[13] G. Kresse and J. Furthmüller, Comput. Mater. Sci. **6**, 15 (1996).

[14] G. Kresse and J. Furthmüller, Phys. Rev. B **54**, 11169 (1996).

[15] G. Kresse and D. Joubert, Phys. Rev. B **59**, 1758 (1999).

[16] J. P. Perdew, K. Burke, and M. Ernzerhof, Phys. Rev. Lett. **77**, 3865 (1996).

[17] The distance between the QL blocks is severely overestimated when using the PBE functional. As positrons are strongly repelled by the ions, the separation between the QL strongly influences the value of the positron work function, and in order to obtain reliable results, we deem it appropriate to work with the experimental lattice parameters instead. The lattice parameters only slightly affect the electronic structure as the results of our band-structure calculations agree very well with the previously reported first-principles results [43,44,51,52] and those of angle-resolved photoemission spectroscopy measurements [53,54].

[18] N. D. Lang and W. Kohn, Phys. Rev. B **7**, 3541 (1973).

[19] R. M. Nieminen and M. J. Puska, Phys. Rev. Lett. **50**, 281 (1983).

[20] We are updating the standard corrugated mirror model for the potential at the surface [19,55,56] where GGA corrections [57] are traditionally not included.

[21] I. Makkonen, M. Hakala, and M. J. Puska, Phys. Rev. B **73**, 035103 (2006).

[22] T. Torsti, M. Heiskanen, M. J. Puska, and R. M. Nieminen, Int. J. Quantum Chem. **91**, 171 (2003).

[23] T. Torsti, T. Eirola, J. Enkovaara, T. Hakala, P. Havu, V. Havu, T. Höynälänmaa, J. Ignatius, M. Lyly, I. Makkonen, T. T. Rantala, J. Ruokolainen, K. Ruotsalainen, E. Räsänen, H. Saarikoski, and M. J. Puska, Phys. Status Solidi B **243**, 1016 (2006).

[24] I. Makkonen, M. Hakala, and M. J. Puska, J. Phys. Chem. Solids **66**, 1128 (2005).

[25] A. Zubiaga, M. M. Ervasti, I. Makkonen, A. Harju, F. Tuomisto, and M. J. Puska, J. Phys. B **49**, 064005 (2016).

[26] R. A. Ferrell, Rev. Mod. Phys. **28**, 308 (1956).

[27] See Supplemental Material at http://link.aps.org/supplemental/10.1103/PhysRevB.94.115411 for a detailed derivation of the formulas.

[28] M. Alatalo, B. Barbiellini, M. Hakala, H. Kauppinen, T. Korhonen, M. J. Puska, K. Saarinen, P. Hautojärvi, and R. M. Nieminen, Phys. Rev. B **54**, 2397 (1996); B. Barbiellini, M. J. Puska, M. Alatalo, M. Hakala, A. Harju, T. Korhonen, S. Siljamäki, T. Torsti, and R. M. Nieminen, Appl. Surf. Sci. **116**, 283 (1997).

[29] N. D. Drummond, P. López Ríos, R. J. Needs, and C. J. Pickard, Phys. Rev. Lett. **107**, 207402 (2011).

[30] R. Saniz, B. Barbiellini, P. M. Platzman, and A. J. Freeman, Phys. Rev. Lett. **99**, 096101 (2007).

[31] E. Zaremba and W. Kohn, Phys. Rev. B **13**, 2270 (1976).

[32] R. Szmytkowski, Phys. Rev. A **65**, 012503 (2001).

[33] S. H. Patil, K. T. Tang, and J. P. Toennies, J. Chem. Phys. **116**, 8118 (2002).

[34] L. Chai, W. Al-Sawai, Y. Gao, A. J. Houtepen, P. E. Mijnarends, B. Barbiellini, H. Schut, L. C. van Schaarenburg, M. A. van Huis, L. Ravelli, W. Egger, S. Kaprzyk, A. Bansil, and S. W. H. Eijt, APL Mater. **1**, 022111 (2013).

[35] K. G. Lynn, W. E. Frieze, and P. J. Schultz, Phys. Rev. Lett. **52**, 1137 (1984).

[36] R. M. Nieminen, M. J. Puska, and M. Manninen, Phys. Rev. Lett. **53**, 1298 (1984).

[37] D. G. Lock, V. H. C. Crisp, and R. N. West, J. Phys. F: Metal Phys. **3**, 561 (1973).

[38] B. Barbiellini, M. J. Puska, A. Harju, and R. M. Nieminen, J. Phys. Chem. Solids **56**, 1693 (1995); A. Shukla, B. Barbiellini, L. Hoffmann, A. A. Manuel, W. Sadowski, E. Walker, and M. Peter, Phys. Rev. B **53**, 3613 (1996).

[39] A. Kawasuso, M. Maekawa, Y. Fukaya, A. Yabuuchi, and I. Mochizuki, Phys. Rev. B **85**, 024417 (2012).

[40] J. A. Weber, A. Bauer, P. Böni, H. Ceeh, S. B. Dugdale, D. Ernsting, W. Kreuzpaintner, M. Leitner, C. Pfleiderer, and C. Hugenschmidt, Phys. Rev. Lett. **115**, 206404 (2015).

[41] J. Henk, A. Ernst, S. V. Eremeev, E. V. Chulkov, I. V. Maznichenko, and I. Mertig, Phys. Rev. Lett. **108**, 206801 (2012).

[42] S. Basak, H. Lin, L. A. Wray, S.-Y. Xu, L. Fu, M. Z. Hasan, and A. Bansil, Phys. Rev. B **84**, 121401 (2011).

[43] H. Lin, T. Das, L. A. Wray, S.-Y. Xu, M. Z. Hasan, and A. Bansil, New J. Phys. **13**, 095005 (2011).

[44] L.-L. Wang and D. D. Johnson, Phys. Rev. B **83**, 241309 (2011).

[45] L. Fu, Phys. Rev. Lett. **103**, 266801 (2009).

[46] S. B. Dugdale, J. Laverock, C. Utfeld, M. A. Alam, T. D. Haynes, D. Billington, and D. Ernsting, J. Phys.: Conf. Ser. **443**, 012083 (2013).

[47] A. Bansil and M. Lindroos, Phys. Rev. Lett. **83**, 5154 (1999); J. C. Campuzano, L. C. Smedskjaer, R. Benedek, G. Jennings, and A. Bansil, Phys. Rev. B **43**, 2788 (1991); J. Nieminen, H. Lin, R. S. Markiewicz, and A. Bansil, Phys. Rev. Lett. **102**, 037001 (2009).

[48] F. Tuomisto and I. Makkonen, Rev. Mod. Phys. **85**, 1583 (2013).

[49] T. R. Devidas, E. P. Amaladass, S. Sharma, R. Rajaraman, D. Sornadurai, N. Subramanian, A. Mani, C. S. Sundar, and A. Bharathi, Europhys. Lett. **108**, 67008 (2014).

[50] S. W. H. Eijt, A. Van Veen, H. Schut, P. E. Mijnarends, A. B. Denison, B. Barbiellini, and A. Bansil, Nat. Mater. **5**, 23 (2006).

[51] X.-Q. Dai, B. Zhao, J.-H. Zhao, Y.-H. Li, Y.-N. Tang, and N. Li, J. Phys.: Condens. Matter **24**, 035502 (2012).

[52] J. Chang, L. F. Register, S. K. Banerjee, and B. Sahu, Phys. Rev. B **83**, 235108 (2011).

[53] M. Neupane, S.-Y. Xu, L. A. Wray, A. Petersen, R. Shankar, N. Alidoust, C. Liu, A. Fedorov, H. Ji, J. M. Allred, Y. S. Hor, T.-R. Chang, H.-T. Jeng, H. Lin, A. Bansil, R. J. Cava, and M. Z. Hasan, Phys. Rev. B **85**, 235406 (2012).

[54] T. Arakane, T. Sato, S. Souma, K. Kosaka, K. Nakayama, M. Komatsu, T. Takahashi, Z. Ren, K. Segawa, and Y. Ando, Nat. Commun. **3**, 636 (2012).

[55] N. G. Fazleev, J. L. Fry, K. H. Kuttler, A. R. Koymen, and A. H. Weiss, Phys. Rev. B **52**, 5351 (1995).

[56] N. G. Fazleev, J. L. Fry, and A. H. Weiss, Phys. Rev. B **70**, 165309 (2004).

[57] B. Barbiellini and J. Kuriplach, Phys. Rev. Lett. **114**, 147401 (2015).